Patient-specific finite element analysis of femurs with cemented hip implants

Yekutiel Katz[a], Omri Lubovsky[b], Zohar Yosibash[a]

[a]*School of Mechanical Engineering, Faculty of Engineering, Tel-Aviv University, Ramat-Aviv, Israel,* *yosibash@tauex.tau.ac.il*

[b]*Department of Orthopedic Surgery, Barzilai Medical Center, Ashqelon, Israel*

Abstract

Background: Over 1.6 million hip replacements are performed annually in Organisation for Economic Cooperation and Development countries, half of which involve cemented implants. Quantitative computer tomography based finite element methods may be used to assess the change in strain field in a femur following such a hip replacement, and thus determine a patient-specific optimal implant. A combined experimental-computational study on fresh frozen human femurs with different cemented implants is documented, aimed at verifying and validating the methods.

Methods: Ex-vivo experiments on four fresh-frozen human femurs were conducted. Femurs were scanned, fractured in a stance position loading, and thereafter implanted with four different prostheses. All femurs were reloaded in stance positions at three different inclination angles while recording strains on bones' and prosthesis' surfaces. High-order FE models of the intact and implanted femurs were generated based on the computer tomography scans and X-ray radiographs. The models were virtually loaded mimicking the experimental conditions and FE results were compared to experimental observations.

Findings: Strains predicted by finite element analyses in all four femurs were in excellent correlation with experimental observations $FE = 1.01 \times EXP - 0.07$, $R^2 = 0.976$, independent of implant's type, loading angle and fracture location.

Interpretation: Computer tomography based finite element models can reliably determine strains on femur surface and on inserted implants at the contact with the cement. This allows to investigate suitable norms to rank implants for a patient-specific femur so to minimize

changes in strain patterns in the operated femur.

Keywords: Total hip arthroplasty, p-FEMs, Femur

1. Introduction

Total hip arthroplasty (THA) is a common procedure, with 1.6 million operations performed annually in the OECD countries (Pabinger and Geissler, 2014). Cemented stems are used in approximately half of the cases (Garellick et al., 2014; Havelin, 2016; Porter, 2016). The metallic stem inserted into the femur changes its natural stress/strain distribution that may lead to bone resorption that is detrimental to mechanical stability (Jayasuriya et al., 2013; Stucinskas et al., 2012).

Implants are usually chosen based on patient's age and bone quality - cemented implants are commonly preferred for older patients. Geometrical compatibility of implant and femur is assured by 2D radiographs or preoperative 3D planning software. Biomechanical aspects as to the strain/stress distribution in the implant-bone compound may prove to be useful in choosing an optimal implant. Such a biomechanical insight is available nowadays by finite element analyses (FEA) that may identify the implant that causes the least deviation in the strain distribution compared to the strain distribution before fracture. Such FEA must first be verified and experimentally validated (Standards, 2006; Henninger et al., 2010) in ex-vivo studies and must demonstrate that the biomechanical response is independent of the type of implant and direction of applied hip contact load. Since strains inside the bone at the interface with the implant cannot be experimentally measured, strain measurements on the implant's surface, being the closest to bone's inner tissue, should be addressed.

FEAs validation studies of implanted femurs were often performed on synthetic femurs (Chen et al., 2013; Stolk et al., 2002; Chen et al., 2004) that do not well represent the complexity of cadaveric femurs (Grant et al., 2007; Zdero et al., 2008). Only few studies validated FEA by experiments on cadaveric femurs. Among these the pioneering study performed three decades ago (Rohlmann et al., 1983) and a comprehensive validation study performed on seven femurs with *cementless* implants Pettersen et al. (2009). In these studies strains were not measured on the stem inside the femur and only one type of prosthesis was

investigated.

Patient-specific high order FEA of intact femurs, based on CT-scans (CTFEA) were verified and double-blind validated in (Trabelsi et al., 2011), and a feasibility study to extend these CTFEAs to a human femur with a cemented prosthesis was successfully completed in (Yosibash et al., 2012). In this study one femur with one implant was studied, and difficulties were encountered in determining the precise location of the implant in the bone and the measurement of the friction load between actuator and implant's head.

To further verify and validate the CTFEA technology for the analysis of implanted femurs we herein consider four femurs with four different cemented implants and present a novel methodology to accurately determine implant's location. Friction forces in one of two directions are eliminated by a new developed experimental jig.

We hypothesize that CTFEAs can reliably predict the mechanical response of a femur with an implant for any femur or implant type, at various hip contact loads applied at different angles. Validating this hypothesis while accounting on measurements performed also inside the femur i.e. on the implant's surface, enhance the reliability of CTFEAs and allows future research so to select an optimal patient specific implant.

2. Methods

Four fresh frozen femurs (National Disease Research Institute, Philadelphia, PA, USA) were implanted with four different cemented prostheses. Donors and prosthesis details are provided in Table 1. Experiments performed on the femurs in both intact and implanted states were simulated by CTFEA and the predicted strains were compared to experimental observations for validation purposes.

2.1. Ex-vivo experiments

All femurs were cleaned of excess fat and soft tissue, distally cut and imbedded 10 cm into a steel cylinder using PMMA. The shaft was aligned with the cylinder axis and the head was placed in the middle of cylinder's square base (see Fig.2). QCT scans were performed by a Phillips Brilliance 64 CT scanner (Eindhoven, Netherlands) at 120 kVp while the femurs are

Table 1: Summary of donor data and prostheses used

Abbrev.	Donor						Prosthesis	
	Gender	Age (years)	Height [cm]	Weight [kg]	L/R	Death cause	Manufacturer	Model
FFM7R	Female	75	162	41	R	cervical cancer	Protec	LOT 2018 7.5 mm
FFB1R	Male	67	178	84	R	heart failure	Protec	LOT 2132 10 mm
FFB1L					L		Groupe Lepine	PAVI H015 0214
FFY	Male	20	185	68	L	drug overdose	Aesculap	ISONIC NK 082 s 8

Scanning parameters

Abbrev.	mAs	Slice thickness & spacing between slices [mm]	Pixel size [mm]	medical center
FFM7R	250	1.25	0.195	Hadassah Ein Kerem
FFB1R	350	1	0.24	Barzilai
FFB1L	300	1	0.3125	Barzilai
FFY	250	1.25	0.336	Hadassah Ein Kerem

immersed in water with five K_2HPO_4 calibration phantoms. Uniaxial strain gauges (SGs) (C2A-06-125 LW-350, Micro Measurements, Raleigh, USA) were bonded on femurs' surface. Additional SGs were bonded to the prostheses prior to implantation. To protect SGs' leads from tearing, the wires were attached to the implant using adhesive. SGs locations are shown in Figure 1.

Loading experiments were performed using the jig shown in Fig. 2. The jig is free to slide in the coronal plane implying zero horizontal force. It consists of a carriage (5) free to slides on four low friction linear bearings and two fitting rail assemblies ($Thomson^{TM}$, Radford, USA) (8). On the carriage, a platform (4) is fixated with two identical pins (6). The platform has four holes to allow its inclination at various angles (0°,7°,15°) representing physiological loading positions (Bergmann et al., 2001). Load was applied by a Shimadzu AG-IC machine (Shimadzu Corporation, Kyoto, Japan) trough a flat actuator pressed against the femoral/implant's head. Forces were measured by a six-axes load cell (ATI Omega 191, Apex, USA), located between the machine's bridge and actuator.

The femurs were anchored to the jig using four bolts at the cylinder's base (see Fig. 2) and thereafter inclined laterally by tilting jig's platform (inclination plane is aligned with femur's

head center and shaft axis). All femurs were loaded to 1500 N at 5 $\frac{mm}{min}$ at 0°,7° and 15° loading configurations. The intact femurs FFB1L and FFB1R were loaded to fracture at 15° inclination at 10 $\frac{mm}{min}$, prior to implantation. FFM7R was loaded to fracture in a past study (Yosibash et al., 2014) and FFY was cut and implanted immediately after the CT scan, no fracture loading was performed on it. Following fracture at the neck in FFB1R, FFB1L and FFM7R and the cut of FFY, the prosthesis was implanted by an orthopedic surgeon. Figure 1 shows the four implanted femurs, the corresponding prostheses and the SGs locations. Figure 3 illustrates the experiments performed on FFB1R and FFB1L. Strains, displacements and load were recorded using a Vishay system 7000 combined with StrainSmart software at a sampling rate of 128 Hz.

Displacements were measured by linear displacement sensors (LDS) (Micro Measurements, Raleigh, USA) The horizontal displacement was measured at the cylinder and vertical was measured at the actuator. To examine femurs' linear elastic response, the strain vs. force was plotted for each SG at each loading configuration. The slope was computed using linear regression (typically between 800 N and 1200 N) and strain value at 1000 N loading was determined from the slope. Each loading was repeated three times to confirm repeatability and the average strain value was used. Same procedure was repeated for the displacements measured by the LDS.

2.2. FE models

Femur's geometry and pointwise material properties were determined from the intact femurs' CT scans following (Yosibash et al., 2007). Since CT scans of the implanted femurs are distorted by the metallic prosthesis, they could not have been used for modeling. Instead, the intact femurs' CTs were manipulated: femurs' models were "cut" at the neck and a CAD model of the implant was virtually inserted (implant's CAD model was obtained by 3D laser digitization prior to implantation).

The steel cylinder plays a key role in the recreation of the experimental conditions, because it has a well defined geometry and configuration both in the experimental setting and in the recreated model. The femur's orientation inside the cylinder defines the boundary conditions

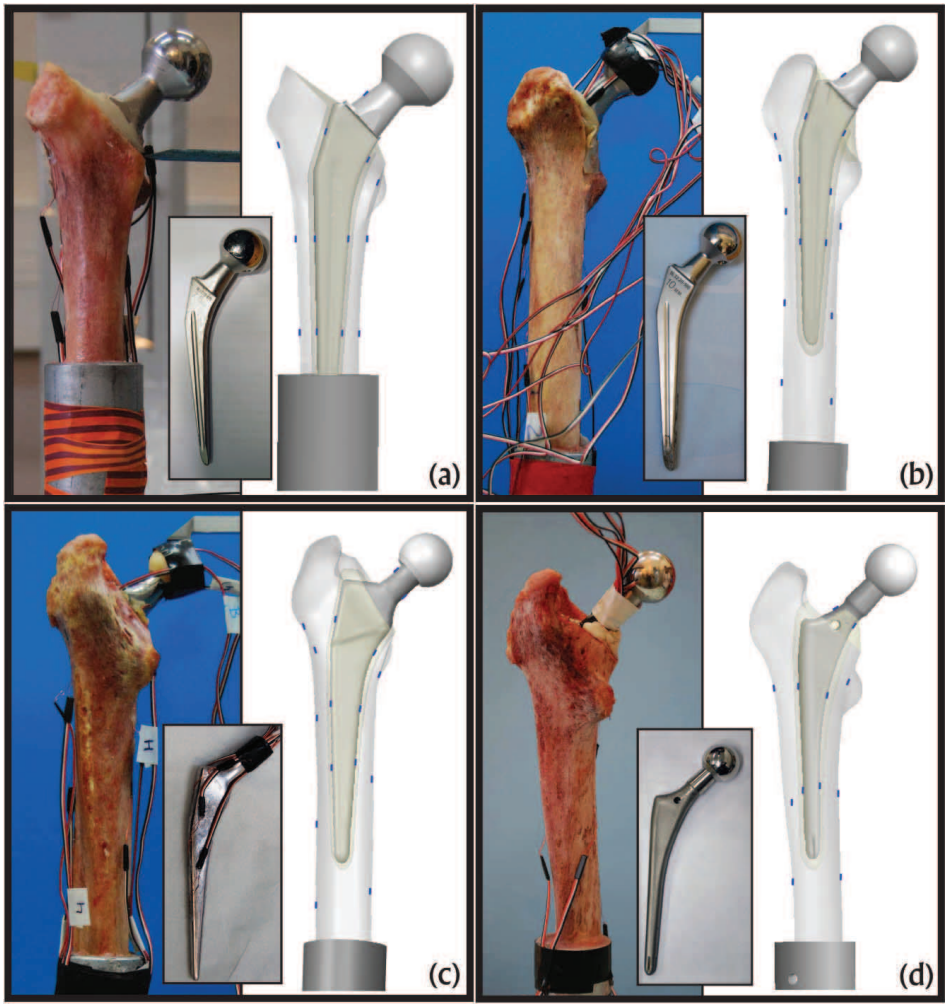

Figure 1: The four implanted femurs, corresponding prostheses and geometric models of cemented THA with SG locations. a) FFM7R b) FFB1R c) FFB1L d) FFY.

and loading directions.

Implanted femurs underwent X-ray radiographs along sagittal and coronal planes (parallel to the square cylinder base). These radiographs were imported into Solidworks (Dassault Systemes SolidWorks Corp, Waltham, USA) and placed onto the corresponding cylinder's planes. The radiographs were aligned with the cylinder and scaled to fit actual dimensions. Femur's CAD model was placed inside the cylinder, so it matches its projections on the two perpendicular radiographs. The implant was also positioned similarly. The entire algorithm is presented in Figure 4.

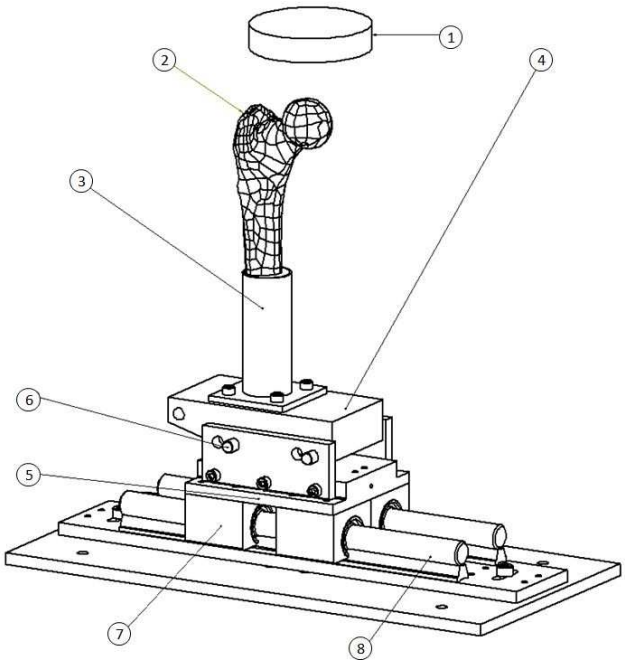

Figure 2: New jig (0° tilt). (1) Machine actuator (2) Fresh frozen bone (3) Steel cylinder (4) Platform (5) Carriage (6) Pins (7) Linear bearings (8) Rails.

Dimensions of the cement layer around the implant are invisible in the CT scan due to artifacts caused by the metallic implant, and are hardly visible in the X-ray images. The cement was assumed to have the same shape as the implant and to be homogenously distributed around it with an average thickness of 3 mm (Isaac et al., 2000). A scaled model of the implant was used to recreate cement's geometry as shown in Fig. 4. The remaining cement outside the femur was modelled based on radiographs and photographs. SG locations on the bone and implant were modelled based on geometrical length measurements. SGs exact orientation and horizontal positioning were assured based on photographs imported into Solidworks and aligned with the CAD model (see Fig. 4).

A sensitivity analysis that quantifies the influence on cement's thickness was performed by considering a FE model with the bone up to the implant (cement thickness layer was set to zero in the model). FE strains at the SG locations where compared between the two models (with and without a cement layer) and the absolute relative difference (relatively to the CTFE model with a cement layer) was computed.

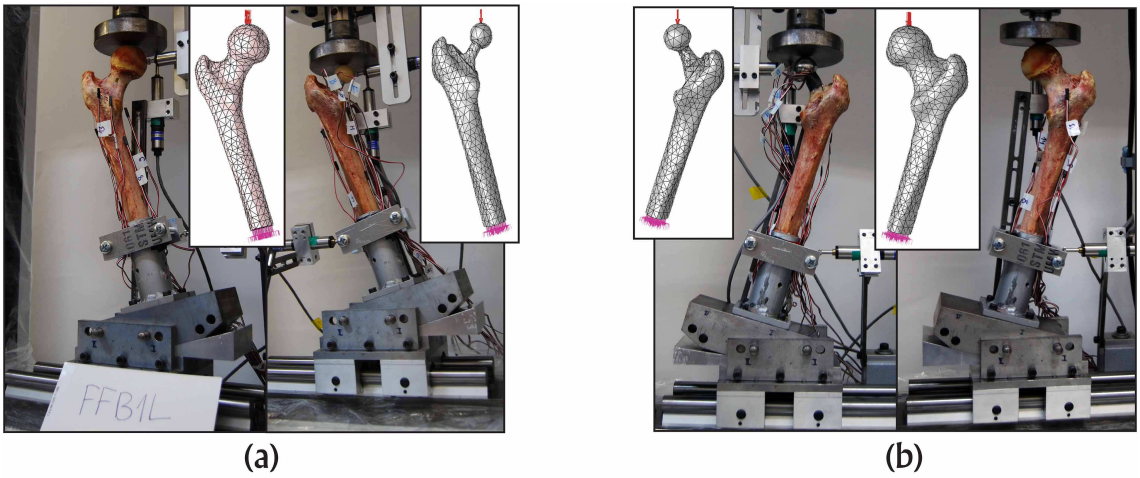

Figure 3: FFB1 loaded at 15^o, Experiment and FE model: (a)FFB1L and FFB1L Imp (b)FFB1R and FFB1R Imp

2.3. CTFE analyses

A tetrahedral mesh was automatically generated resulting in 7500 to 10000 tetrahedrons for the implanted femurs (1.4-2.5 million degrees of freedom (DOF) at p=8) and about 4000 elements for the intact femurs (about 1 million DOF at p=8).

Analysis of the QCT scan calibration phantoms' density and HUs resulted in:

$$\rho_{K_2HPO_4} = 10^{-3}\ (0.8 \cdot HU), \tag{1}$$

Ash density ρ_{ash} was determined based on $\rho_{K_2HPO_4}$ according to relations obtained in Faulkner et al. (1993) ($\rho_{K_2HPO_4}$ to ρ_{HA}) and Schileo et al. (2008) (ρ_{HA} to ρ_{ash}) :

$$\rho_{ash} = (0.877 \times 1.15 \times \rho_{K_2HPO_4} + 0.08)[gr/cm^3] \tag{2}$$

Following (Yosibash et al., 2012, 2014), an inhomogeneous isotropic Hooke's model was used depending on ρ_{ash}:

$$E_{cort} = 10200 \cdot \rho_{ash}^{2.01}\ [MPa], \qquad \rho_{ash} > 0.486 \tag{3}$$

$$E_{trab} = 2398\ [MPa], \qquad 0.3 < \rho_{ash} \leq 0.486$$

$$E_{trab} = 33900 \cdot \rho_{ash}^{2.2}\ [MPa], \qquad \rho_{ash} \leq 0.3 \tag{4}$$

where E_{cort} and E_{trab} are Young's moduli for cortical and trabecular bone respectively.

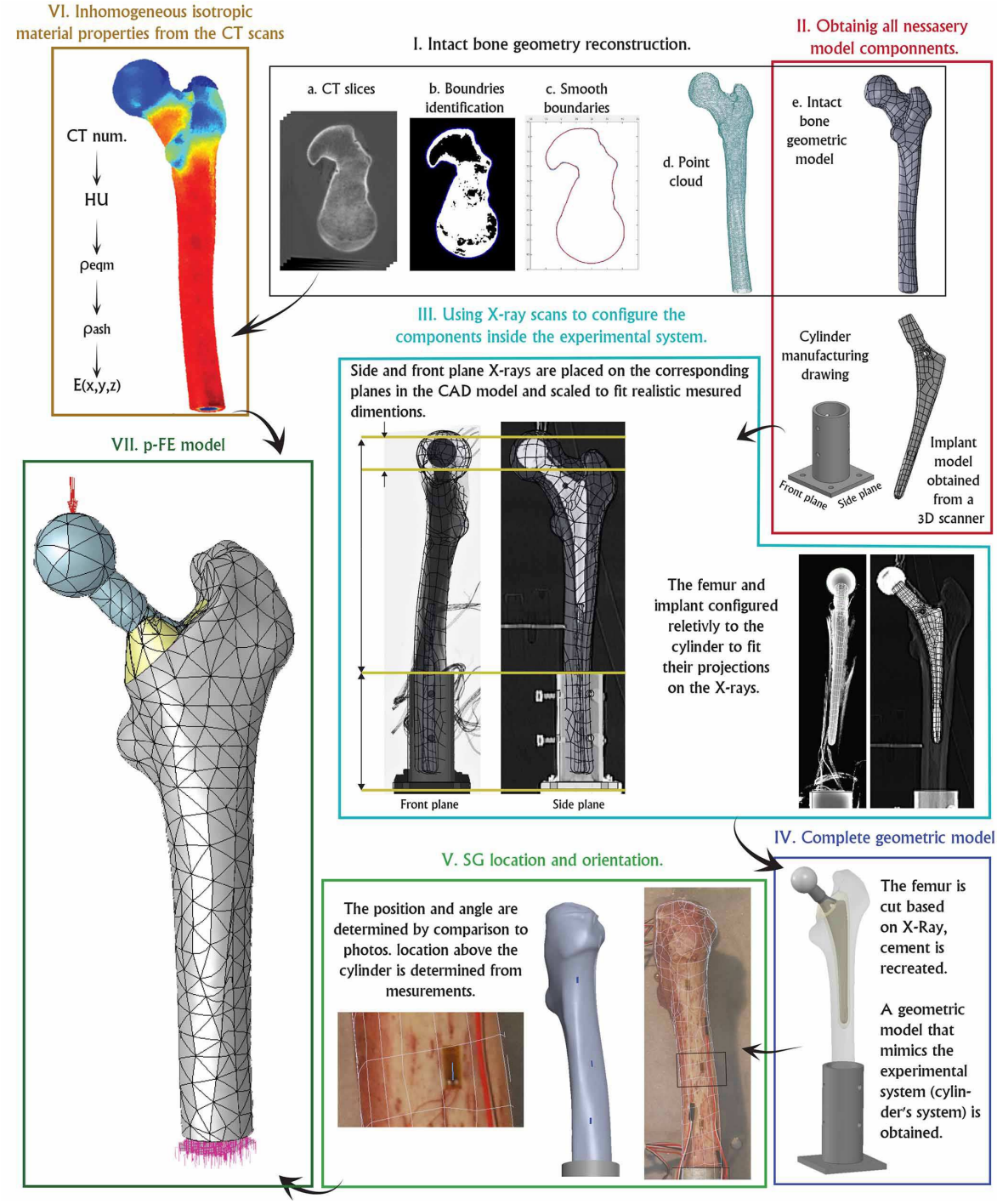

Figure 4: Construction algorithm of the CTFE model.

Poisson's ratio was taken as 0.3.

Material properties of the implants were found as follows: Density was calculated based

on the volume obtained from a 3D laser scan and their mass (7.85 gr/cc typical to stainless steel). In addition, energy dispersive X-ray analysis (EDXA) was performed on one implant showing a chemical composition of a high quality stainless steel: 22.19% Cr and 8.88% Ni. Following these observations, mechanical properties typical to stainless steel were assigned to the implant: $E_{Imp} = 200$ GPa, ν=0.3.

Cement's Young modulus was determined by compression experiment conducted on cylindrical specimens created from same cement used during implantation, resulting in $E = 2.7$ GPa and ν=0.3. In all CTFE models the implant was perfectly bonded to the cement that was perfectly bonded to the bone.

A 1000N load was applied to head's surface at 0°,7° and 15°. The direction of the load and inclination plane were defined relatively to the upper cylindrical steel surface (cylinder not included in the FE model). The femur was clamped at the distal end of the shaft. In the experiment the distal shaft could slide laterally, while the head position remained constant under the actuator. In the CTFE model we fully constrained the distal shaft and applied no constrain on the head. These boundary conditions are equivalent.

Linear FE analyses were performed by increasing the polynomial degree (from 6 to 8) using StressCheck software (ESRD, St. Louis, USA). Once ensuring that the error in energy norm had converged, strain convergence was confirmed at the SG locations, and principal strains were extracted and averaged along the length of each SG.

2.4. Analysis of results

Strains measured by the SGs were compared to the ones predicted by the CTFEA. Most SGs were well aligned along the principal strain direction. Displacements were extracted and averaged on the loading surface at the head.

To quantify the agreement, linear correlation (LC) and Bland-Altman (BA) plots (Bland and Altman, 1986) were generated. The root-mean-square error (RMSE) was also calculated. In BA plots the y-axis represents the difference in absolute principle strain values so that positive values represent larger strains in experiment (stiffer CTFE model) whereas negative values represent a "softer" CTFE model.

The yield load of the intact femurs FFB1L, FFB1R and FFM7R (yielding was noticed before fracture) was measured and is provided in Appendix A in the Supplementary material.

To quantify the effect of the cement layer on the predicted SG strains, absolute relative difference and RMSE between the fully cemented and zero cemented models was calculated:

$$RMSE = \sqrt{\frac{\sum_{1}^{N}(\varepsilon_{cemented} - \varepsilon_{noncemented})^2}{N}} \tag{5}$$

where N is the number of SG data available (number of SG times the number of loading inclinations).

To quantify the change in the biomechanical conditions following the insertion of the implant, Relative (Rel) and absolute (Abs) change in principal strains was calculated. The calculation was performed at the implant's mid-plane, while addressing tensile strains at the lateral side of the femur and compressive strains at the medial side. The compuation was performed using: (6-7):

$$Abs = \left|Intact_{\varepsilon_{1/3}}\right| - \left|Implant_{\varepsilon_{1/3}}\right| \quad \text{Absolute Diff} \tag{6}$$

$$Rel = \frac{Intact_{\varepsilon_{1/3}} - Implant_{\varepsilon_{1/3}}}{Intact_{\varepsilon_{1/3}}} \quad \text{Relative Diff} \tag{7}$$

where $Intact_{\varepsilon_{1/3}}$ and $Implant_{\varepsilon_{1/3}}$ are maximum principal strains before and after implantation.

3. Results

A linear response between load and measured strains was observed in the experiments for all femurs at all inclination angles with a linear regression coefficient $R^2 > 0.99$. The three repeated loads at all configuration showed high repeatability: strains typically varied by 10-20 $\mu strain$ between repetitions.

All FE models were monitored so to ensure an error in energy norm below 6% at $p = 8$. Strain converged to ∼1% relative error between consecutive FEAs. Figure 5 shows the FE mesh and principal strains on the four implanted femurs.

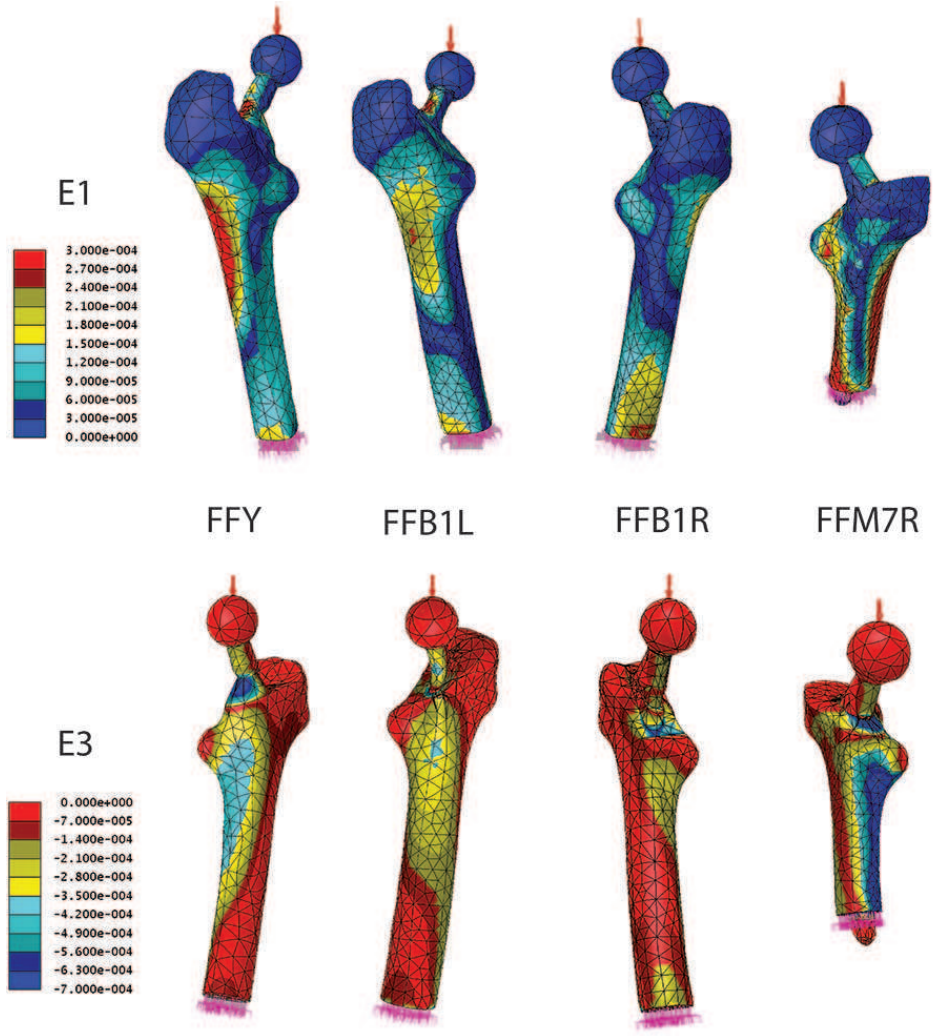

Figure 5: The four FE meshes for the implanted femurs (cement modelled) loaded at 15^o and the maximum (top) and minimum (bottom) principal strains.

The linear correlation and RMSE between experiments and CTFEA is presented in equation (8) for the two intact femurs and in equation (9) for the four implanted ones. The BA and LC plots are shown in Figure 6.

$$FE = 0.979 \times EXP - 5.44 \quad (R^2 = 0.987), \quad RMSE = 95 \quad [\mu strain] \tag{8}$$

$$FE = 1.01 \times EXP - 0.07 \quad (R^2 = 0.976), \quad RMSE = 84 \quad [\mu strain] \tag{9}$$

The LC obtained for each experiment separately is detailed in the following, plots and detailed results for each SG and every loading condition are summarized in Appendix B.

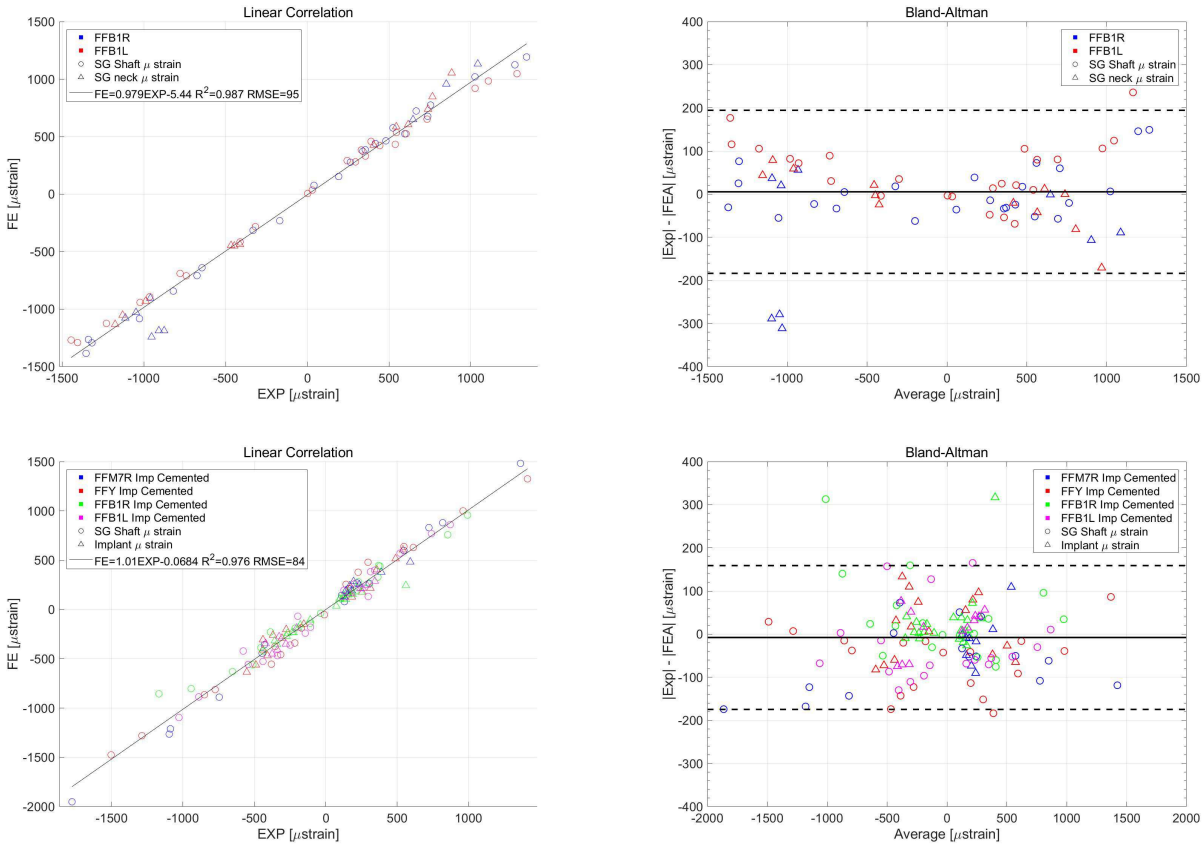

Figure 6: LC and BA plots including data of all intact (Top) and all implanted femurs (Bottom). All models include the cement.

FE [μ strain]= $a\times$ EXP $+b$, where

Femur	a	b	R^2
FFB1R	1.02	-25.2	0.987
FFB1L	0.935	13.6	0.993
FFM7R Imp	1.09	-4.56	0.994
FFB1R Imp	0.873	2.99	0.968
FFB1L Imp	1.02	-12.3	0.972
FFY Imp	1.02	2.02	0.981

The FE results for models with cement at the bone-implant interface were compared to the ones without. A mean absolute difference of 4.2% and RMSE of 32.7 μstrain were obtained accounting for all femurs and all locations. Analyzing implant and bone strains separately, one obtains a difference of 2.4% (RMSE = 6.6 μstrain) for the implant strains

and 5.4% (RMSE = 42.6 μstrain) for bone strains. The linear correlation between the strains in the cemented and non-cemented models resulted in a slope of 0.996, intersection of 6.39 and $R^2 = 0.975$

Figure 7 illustrates the relative and absolute differences in principal strains following implant insertion for FFB1R at 7^0 loading, demonstrating a decrease in strains in almost all areas.

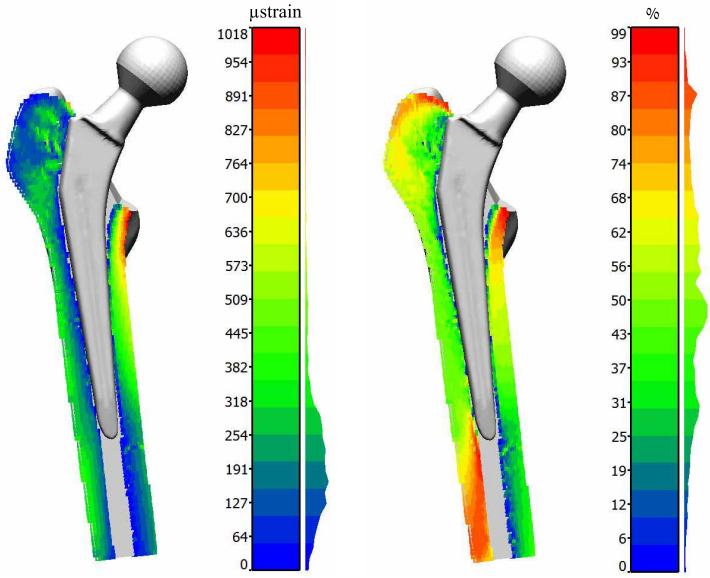

Figure 7: Strain shielding quantification for FFB1R at 7^0 loading using a simplified model which does not include the cement layer. Left: Absolute difference in principal strains (6). Right: Relative difference in principal strains (7).

4. Discussion

To the best of our knowledge, only a scarce number of studies presented verified and validated CTFE models of fresh-frozen human femurs with cemented prostheses. Herein methods for the analysis of implanted femurs by high order FE methods were improved and validated by ex-vivo experiments on four fresh frozen femurs with different prostheses. A construction methodology to determine the prosthesis location within the femur was presented. An excellent correlation was obtained between experimental observations and FE predictions for each of the implanted and intact femurs considering all three loading angles. The overall

agreement for all intact femurs was: $FE = 0.979 \times EXP - 5.44,\ R^2 = 0.976$ and for all implanted ones was: $FE = 1.01 \times EXP - 0.07,\ R^2 = 0.976$. The slope values are close to one and the intersection is close to zero. The RMSE between the experimental results and the predicted values was less then 100 μstrain while the strain values were $\pm 1500\mu$strain. No bias was observed In the BA plots (average error is close to zero) and the standard deviation of the differences (random fluctuations) is small relatively to the mesuered/predicted values.

Validation is enhanced following our former study, where a single implanted femur was used (Yosibash et al., 2012) and the lateral force has been assumed since it was not measured. The improvements in the experimental system and the accurate CTFE model construction in the current study improves the reliability of the predicted strains. The cohort of different femurs and implants used for validation is also significantly increased (five in total), further demonstrating that the model is femur/implant independent.

The cement modelling had negligible effect on the strains predicted at the SG locations, attributed to the similarity in stiffness between the cement and the bone tissue. Both CTFE models, with and without cement, were in good agreement with the experimental measurements. This suggests that a simplified CTFE model, where the cement thickness is zero, may be sufficient for experimental validation. Moreover, because the cement distribution cannot be known preoperatively, such a simplified FE model may be a reasonable approximation and might well serve for implant comparison and choice prior to implantation. Factors such as implant's geometry and material are presumably much more dominant in their biomechanical effect than the cement thickness - factors that will be verified in a future work.

Once patient specific CTFE models were shown to well predict the mechanical response of both intact and implanted femurs (Yosibash et al., 2012; Trabelsi et al., 2011), these may provide quantitative measures on the strain alteration due to the presence of an implant, i.e. quantify strain-shielding. However, several different stress/strain-shielding measures exist: some based on von Mises stresses (Yamako et al., 2014; Joshi et al., 2000; Pettersen et al., 2009; Hirata et al., 2013), some based on von Mises strains (Pettersen et al., 2009), some based on strain energy density (Yamako et al., 2014) and some based on the principal strains (Cilla et al., 2017). In many cases these measures are computed on bone or implant surfaces

rather than inside the femur and changes between the intact and implanted configurations are not quantified but qualitatively discussed.

Relative changes and absolute differences in principal strains between the intact implanted femur was presented in Figure 7 for FFB1R at 7^0 loading. Similarly to Gruen zones (Gruen et al., 1979) commonly used in clinical practice to qualitatively evaluate bone mineral density (BMD) resorption, one may consider different volumes/areas as in Figure 7 to quantify the strain shielding effects and minimize them by a proper implant. Herrera et al. (Herrera et al., 2014) monitored patients after cemented prostheses (two kinds) and reported that BMD decreased in all Gruen zones post prosthesis implantation (Fig. 4 in (Herrera et al., 2014)). Jayasuriya et al. (Jayasuriya et al., 2013) reported on a decrease in BMD over the first year with greatest loss of 14% in the proximal medial femur (Gruen zone 7). Stucinskas et al. (Stucinskas et al., 2012) report on a significant decrease in cortical thicknesses in total hip arthroplasty at all periprosthetic levels but less expressed distally. These clinical observations are coherent with our FE predictions: one notices in Fig. 7 that maximum principal strain decreased everywhere around the prosthesis.

The verified and validated (V&V) high order FE technique presented herein is a first essential step to reliably address strain shielding by FEA. An appropriate norm to quantify strain shielding has still to be determined and validated by comparison to clinical observations, which is a topic of future investigation.

There are two limitations of our study. Validation of CTFE results was performed on the basis of a limited number of locations at which principal strains were measured. Vertical measured displacements were consistently larger than CTFE predictions due to movement of the distal part of femur's shaft placed within the PMMA. Future experiments will use a digital image correlation system that will allow thousands of locations to be compared. Linear and isotropic material properties were shown to be appropriate for FEA of intact femurs (Trabelsi et al., 2011; Trabelsi and Yosibash, 2011). This assumption should be re-evaluated for implanted femurs.

5. Conclusions

A high order CTFE model simulating the prosthesis location within the femur was presented and validated by experimentation. An excellent correlation of CTFE strains on femur's and prosthesis' surfaces (inside the bone) to experimental observations was obtained for the different femurs and implants examined. This allows the use of the validated CTFE models to investigate strain-shielding effects in these locations within the bone that cannot be accessed by any experimental measurement system. An appropriate norm to quantify strain shielding has still to be determined and validated by comparison to clinical observations, which is a topic of future investigation.

Conflict of Interest

YK and OL have no conflicts of interest. ZY has a financial interest in PerSimiO.

Acknowledgements

The authors gratefully acknowledge the anonymous referees for valuable and constructive comments, leading to improvements in the presentation and context.

The authors thank Prof. Charles Milgrom, from the Hadassah Hospital for assistance with insertion the prosthesis in FFY. The authors also thank Prof. Moshe Salai from Sourasky medical center and Mr. Ilan Gilad and Ms. Gal Dahan from the Tel-Aviv University for their assistance. This study was made possible through the generous support of a Milgrom Foundation for Science grant.

References

Bayraktar, H., Morgan, E., Niebur, G., Morris, G., Wong, E., Keaveny, M., 2004. Comparison of the elastic and yield properties of human femoral trabecular and cortical bone tissue. Jour. Biomech. 37, 27–35.

Bergmann, G., Deuretzbacher, G., Heller, M.O., Graichenm, F., Rohlmann, A., Strauss, J., Haas, N.P., Duda, G., 2001. Hip contact forces and gait patterns from routine activities. Jour. Biomech. 34, 859 – 871.

Bland, J., Altman, D., 1986. Statistical methods for assessing agreement between two methods of clinical measurement. Lancet 1, 307 – 310.

Chen, D., Lin, C., Hu, C., Tsai, M., Lee, M., 2013. Biomechanical consideration of total hip arthroplasty following failed fixation of femoral intertrochanteric fractures - a finite element analysis. Medical Engineering & Physics 35, 569–575.

Chen, W., Tai, C., Lee, M., Lee, P., Liu, C., Shih, C., 2004. Comparison of stress shielding among different cement fixation modes of femoral stem in total hip arthroplasty a three dimensional finite element analysis. Journal of Medical and Biological Engineering 24, 183–188.

Cilla, M., Checa, S., Duda, G., 2017. Strain shielding inspired re-design of proximal femoral stems for total hip arthroplasty. Journal of Orthopaedic Research .

Faulkner, K.G., GlÃŒer, C.C., Grampp, S., Genant, H.K., 1993. Cross-calibration of liquid and solid qct calibration standards: Corrections to the ucsf normative data. Osteoporosis International 3, 36 – 42.

Garellick, G., Karrholm, J., Lindahl, H., Malchau, H., Rogmark, C., Rolfson, O., 2014. Swedish hip arthroplasty register, annual report 2014. URL: http://www.shpr.se/Libraries/Documents/Annual_Report_2014_Eng.sflb.ashx.

Grant, J., Bishop, N., Gotzen, N., Sprecher, C., Honl, M., Morlock, M., 2007. Artificial composite bone as a model of human trabecular bone: The implant bone interface. Jour. Biomech. 40, 1158–1164.

Gruen, T., Mcneice, G., Amstutz, H., 1979. Modes of failure of cemented stem–type femoral components: A radiographic analysis of loosening. Clinical Orthopaedics and Related Research: 141, 17–27.

Havelin, L., 2016. Report 2016 - Norwegian National Advisory Unit on Arthroplasty and Hip Fractures. URL: http://nrlweb.ihelse.net/Rapporter/Report2016_english.pdf.

Henninger, H., Reese, S., Anderson, A., Weiss, J., 2010. Validation of computational models in biomechanics. Proceedings Of The Institution Of Mechanical Engineers Parft H-Journal Of Engineering In Medicine 224, 801–812.

Herrera, A., Rebello, S., Ibarz, E., Mateo, J., ans L. Garcia, S.G., 2014. Mid-term study of bone remodeling after femoral cemented stem implantation: Comparison between dxa and finite element simulation. J. Arthroplasty 29, 90–100.

Hirata, Y., Inaba, Y., Kobayashi, N., Ike, H., Fujimaki, H., T.Saito, 2013. Comparison of mechanical stress and change in bone mineral density between two types of femoral implant using finite element analysis. J. Arthroplasty 28, 1731–5.

Isaac, G., Busch, C., Shetty, V., Drabu, K., 2000. Radiographic assessment of the cement mantle thickness of the femoral stem in total hip replacement: a case study of 112 consecutive implants. Proc Instn Mech Engrs 214, 471–477.

Jayasuriya, R., Buckley, S., Hamer, A., Kerry, R., Stockley, I., Tomouk, M., Wilkinson, J., 2013. Effect of sliding-taper compared with composite-beam cemented femoral prosthesis loading regime on proximal femoral bone remodeling: a randomized clinical trial. Jour. Bone Joint Surgery - Americal Volume 95A, 19–27.

Joshi, M., Advani, S., Miller, F., Santare., M.H., 2000. Analysis of a femoral hip prosthesis designed to reduce stress shielding. Journal of Biomechanics 33, 1655–62.

Pabinger, C., Geissler, A., 2014. Utilization rates of hip arthroplasty in oecd countries. Osteoarthritis and Cartilage 22, 734–741.

Pettersen, S., Wik, T., Skallerud, B., 2009. Subject specific finite element analysis of stress shielding around a cementless femoral stem. Clin. Biomech. 24, 196–202. 1st Corrigendum, Clin. Biomech., **24**(8), 2009, p. 697. 2nd Corrigendum, Clin. Biomech., **26**(4), 2011, p. 429.

Porter, M., 2016. National Joint Registry for England, Wales, Northern Ireland and the Isle of Man. URL: `http://www.njrreports.org.uk/Portals/0/PDFdownloads/NJR\%2012th\%20Annual\%20Report\%202015.pdf`.

Rohlmann, A., Mossner, U., Bergmann, G., Kolbel, R., 1983. Finite-element-analysis and experimental investigation in a femur with hip endoprosthesis. Journal of Biomechanics 16, 727–742.

Schileo, E., DallAra, E., Taddei, F., Malandrino, A., Schotkamp, T., Baleani, M., Viceconti, M., 2008. An accurate estimation of bone density improves the accuracy of subject-specific finite element models. Jour. Biomech. 41, 2483–2491.

Standards, A., 2006. ASME V&V 10 – 2006 Guide for Verification and Validation in Computational Solid Mechanics. The American Society of Mechanical Engineers, New York.

Stolk, J., Verdonschot, N., Cristofolini, L., Toni, A., Huiskes, R., 2002. Finite element and experimental models of cemented hip joint reconstructions can produce similar bone and cement strains in pre-clinical tests. Journal of Biomechanics 35, 499–510.

Stucinskas, J., Clauss, M., Tarasevicius, S., Wingstrand, H., Ilchmann, T., 2012. Long-term femoral bone remodeling after cemented hip arthroplasty with the Muller straight stem in the operated and nonoperated femora. The Journal of Arthroplasty 27, 927 – 933.

Trabelsi, N., Yosibash, Z., 2011. Patient-specific FE analyses of the proximal femur with orthotropic material properties validated by experiments. ASME Jour. Biomech. Eng. 155, 061001–1 – 061001–11.

Trabelsi, N., Yosibash, Z., Wutte, C., Augat, R., Eberle, S., 2011. Patient-specific finite element analysis of the human femur - a double-blinded biomechanical validation. Jour. Biomech. 44, 1666 – 1672.

Yamako, G., Chosa, E., Zhao, X., Totoribe, K., Watanabe, S., Sakamoto, T., Nakane, N., 2014. Load-transfer analysis after insertion of cementless anatomical femoral stem using pre- and post-operative ct images based patient-specific finite element analysis. Medical Engineering and Physics 36, 694–700.

Yosibash, Z., Katz, A., Milgrom, C., 2012. Toward verified and validated FE simulations of a femur with a cemented hip prosthesis. Medical Engineering & Physics 35, 978–987.

Yosibash, Z., Plitman Mayo, R., Dahan, G., Trabelsi, N., Amir, G., Milgrom, C., 2014. Predicting the stiffness and strength of human femurs with real metastatic tumors. Bone 69, 180–190.

Yosibash, Z., Tal, D., Trabelsi, N., 2010. Predicting the yield of the proximal femur using high order finite element analysis with inhomogeneous orthotropic material properties. Philosophycal Transaction of the Royal Society: A 368, 2707–2723.

Yosibash, Z., Trabelsi, N., Milgrom, C., 2007. Reliable simulations of the human proximal femur by high-order finite element analysis validated by experimental observations. Jour. Biomech. 40, 3688–3699.

Zdero, R., Olsen, M., Bougherara, H., Schemitsch, E., 2008. Cancellous bone screw purchase: A comparison of synthetic femurs, human femurs, and finite element analysis. Eng. Med. 222, 1175–1183.

Appendix A. Yield load for the intact femurs

The yield load of the intact femurs FFB1L, FFB1R and FFM7R (yielding was noticed before fracture) was defined as the maximum recorded load before a deviation in the strain-force slope occurs. In the FEA, the yield load was computed by the failure criterion based on a linear elastic analysis and maximum principal strain on bone surface as documented in (Yosibash et al., 2010). The yield load in stance position is the load resulting in a maximum principal strain in tension equal to 7300 μstrain (Bayraktar et al., 2004).

FFB1L and FFB1R, loaded at 15^o, experienced yielding at the neck at $\sim$8100 N and 7600 N and brittle-like tensile fracture at 8600 and 8100 N respectively. The FEA predicted yielding loads of 7100 to 7300 N. FFM7R was fractured in a previous study, experiencing yielding at 4800 N and fractured at 5300 N whereas the FE predicted yielding was 3730 N (Table 6 in (Yosibash et al., 2014)). Force vs strain plot for all three fractured bones is shown in Figure A.8. The presented strains were measured by the SGs closest to the fracture initiation location.

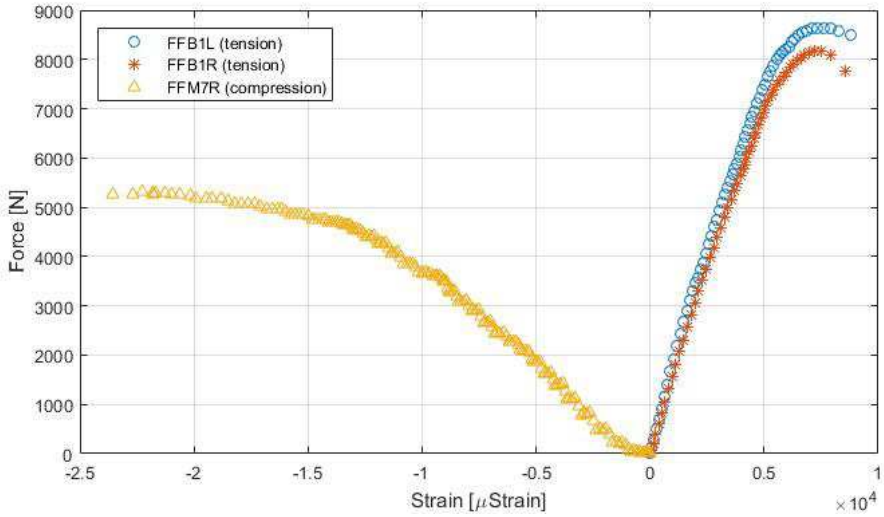

Figure A.8: Strains measured during fracture loading at the SG located closest to the fracture. Data for FFM7R was taken form (Yosibash et al., 2014)

The predicted yield load to fracture for the intact femurs FFB1L, FFB1R and FFM7R underestimated the experimental observation by 12.5%, 17% and 22%, respectively.

Appendix B. Experimental data and FE results

This appendix summarizes all measured strains and displacements and the corresponding QCT-FE results. Some of the SGs were damaged during prosthesis implantation so no data was recorded and some SGs were not bonded properly. These are marked blue and their data is discarded. Some SGs were boned at neck's neutral axis and report on small strains, and in the FE analysis a very high sensitivity of the results to SG location in the FE model was noticed - these were also discarded and marked blue. We also discard displacements since the FE model does not represent the PMMA and cylindrical sleeve so measured and experimental displacements cannot be well simulated.

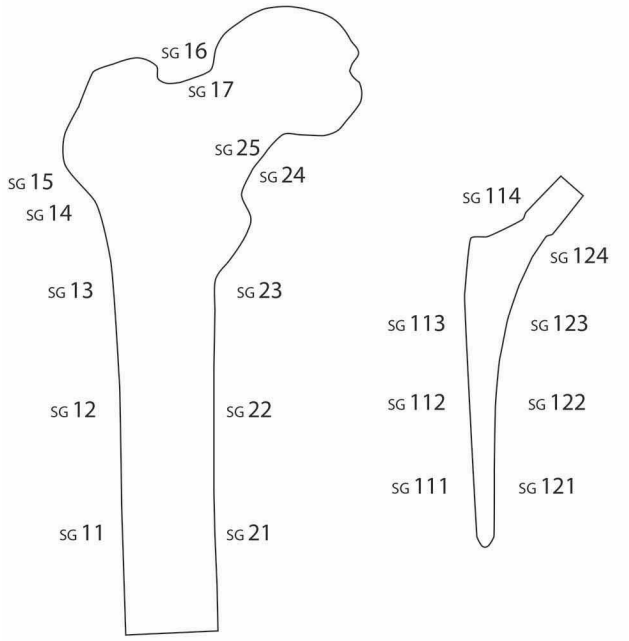

Figure B.9: Strain gauge notations for femurs and prostheses

Table B.2: FFM7R Imp: Experimental observations and FE results at 1000 N load.

	Strain [μstrain]													Disp [μm]	
	SG 11	**SG 12**	**SG 13**	**SG 21**	**SG 22**	**SG 23**	**SG 111**	**SG 112**	**SG 113**	**SG 114**	**SG 121**	**SG 122**	**SG 123**	**Uz**	**Ux**
							0° loading								
Exp	1364	819	218	-1777	-1097	-81	-	592	194	181	-	-	-	-756	2040
FE	1483	881	270	-1952	-1265	-728	-	482	285	191	-	-	-	-420	1188
Diff %	-9	-8	-24	-10	-15	-802	-	18	-47	-6	-	-	-	44	42
							7° loading								
Exp	722	548	160	-1088	-746	-55	-	389	168	154	-	-	-	-376	1088
FE	831	598	212	-1211	-889	-618	-	378	241	163	-	-	-	-218	793
Diff %	-15	-9	-33	-11	-19	-1026	-	3	-44	-6	-	-	-	42	27
							15° loading								
Exp	131	305	109	-430	-446	-37	-	235	138	127	-	-	-	-152	-12
FE	80	264	143	-357	-444	-489	-	252	187	128	-	-	-	-87	292
Diff %	39	13	-30	17	1	-1210	-	-7	-35	-1	-	-	-	43	2446

Table B.3: FFB1R Imp: Experimental observations and FE results at 1000 N load.

	Strain [μstrain]														Disp [μm]	
	SG 11	SG 12	SG 13	SG 14	SG 21	SG 22	SG 23	SG 111	SG 112	SG 113	SG 115	SG 121	SG 122	SG 123	Uz	Ux
								0° loading								
Experiment	993	854	380	39	-1169	-943	-654	301	561	151	189	-343	-357	-275	-494	2162
FE	958	758	440	235	-856	-803	-630	265	244	178	179	-353	-316	-271	-354	1437
Diff %	3	11	-16	-507	27	15	4	12	57	-17	5	-3	11	1	28	34
								7° loading								
Experiment	227	365	228	27	-388	-454	-439	187	249	127	156	-225	-268	-236	-191	405
FE	226	329	282	179	-228	-388	-420	155	177	145	149	-235	-241	-233	-117	614
Diff %	0	10	-23	-565	41	15	4	17	29	-15	5	-5	10	1	39	-52
								15° loading								
Experiment	-511	-109	105	24	370	-36	-215	74	141	97	122	-109	-179	-193	-202	849
FE	-561	-139	108	116	446	-38	-189	35	102	108	114	-106	-156	-188	-85	-304
Diff %	-10	-28	-3	-381	-20	-5	12	52	27	-12	7	2	13	2	58	136

Table B.4: FFB1L Imp: Experimental observations and FE results at 1000 N load.

	Strain [μstrain]														Disp [μm]	
	SG 11	SG 12	SG 13	SG 14	SG 15	SG 21	SG 22	SG 23	SG 111	SG 112	SG 114	SG 121	SG 122	SG 124	Uz	Ux
								0° loading								
Experiment	871	740	520	11	38	-1029	-890	-338	-	343	288	-	-421	-376	-279	1716
FE	861	770	572	171	192	-1096	-887	-468	-	287	247	-	-344	-451	-352	1275
Diff %	1	-4	-10	-1482	-404	-7	0	-38	-	16	14	-	18	-20	-26	26
								7° loading								
Experiment	203	314	342	8	14	-440	-543	-250	-	258	243	-	-327	-339	-178	132
FE	263	384	398	147	137	-527	-558	-361	-	216	211	-	-275	-409	-140	675
Diff %	-29	-22	-16	-1822	-857	-20	-3	-44	-	16	13	-	16	-21	21	-412
								15° loading								
Experiment	-579	-196	127	7	-6	297	-107	-144	-	133	178	-	-204	-280	-157	-750
FE	-421	-68	195	111	80	132	-179	-240	-	126	163	-	-187	-349	-61	-55
Diff %	27	65	-54	-1551	1484	56	-67	-67	-	6	8	-	8	-25	61	93

Table B.5: FFY Imp: Experimental observations and FE results at 1000 N load.

	Strain [μstrain]												Disp [μm]	
	SG 11	SG 12	SG 13	SG 21	SG 22	SG 23	SG 111	SG 112	SG 113	SG 121	SG 122	SG 123	Uz	Ux
							0° loading							
Experiment	1412	961	296	-1504	-1288	-381	-	313	540	-441	-440	-554	-985	1413
FE	1326	1001	480	-1475	-1281	-555	-	216	605	-410	-307	-636	-644	2066
Diff %	6	-4	-62	2	1	-46	-	31	-12	7	30	-15	35	-46
							7° loading							
Experiment	613	547	227	-775	-850	-315	-	256	489	-307	-370	-490	-404	1313
FE	629	639	378	-813	-865	-458	-	176	516	-290	-260	-562	-273	1250
Diff %	-3	-17	-67	-5	-2	-45	-	31	-6	6	30	-15	32	5
							15° loading							
Experiment	-171	174	142	-10	-355	-217	-	183	357	-154	-277	-408	-228	-162
FE	-188	215	255	-53	-375	-340	-	128	404	-148	-203	-468	-93	238
Diff %	-10	-24	-80	-428	-6	-57	-	30	-13	4	27	-15	59	247

Table B.6: FFB1R (Intact): Experimental observations and FE results at 1000 N load. SG18 data was discarded because it is located at the highest point of the neck and the CT-scan slices above and below it are too far apart to contain the cortex. As a result the FE model at this point has no cortex properties and FE strain there is unrealistically large.

	Strain [μstrain]													Disp [μm]	
	SG 11	**SG 12**	**SG 13**	**SG 14**	**SG 15**	**SG 21**	**SG 22**	**SG 23**	**SG 16**	**SG 17**	**SG 18**	**SG 24**	**SG 25**	**Uz**	**Ux**
							0° **loading**								
Experiment	1342	1271	1026	666	416	-1340	-1318	-1354	1043	148	799	-1114	-953	-1008	-
FE	1193	1125	1020	723	441	-1264	-1293	-1385	1133	63	1525	-1077	-1242	-786	-
Diff %	11	11	1	-9	-6	6	2	-2	-9	57	-91	3	-30	22	-
							7° **loading**								
Experiment	597	737	754	524	340	-645	-821	-1028	851	68	651	-1049	-909	-516	1538
FE	525	677	775	576	373	-640	-843	-1083	957	-47	1292	-1029	-1188	-407	1374
Diff %	12	8	-3	-10	-10	1	-3	-5	-13	169	-98	2	-31	21	11
							15° **loading**								
Experiment	-169	192	481	355	263	41	-332	-675	647	-56	470	-961	-877	-307	93
FE	-231	153	464	386	278	77	-314	-709	648	-142	956	-905	-1188	-188	356
Diff %	-37	20	4	-9	-5	-88	5	-5	0	-154	-103	6	-36	39	-283

Table B.7: FFB1L (Intact): Experimental observations and FE results at 1000 N load.

	Strain [μstrain]													Disp [μm]	
	SG 11	**SG 12**	**SG 13**	**SG 15**	**SG 14**	**SG 21**	**SG 22**	**SG 23**	**SG 16**	**SG 17**	**SG 24**	**SG 25**	**SG 26**	**Uz**	**Ux**
							0° **loading**								
Experiment	1284	1108	1027	390	546	-1446	-1407	-1230	884	739	-1177	-467	-82	-995	2421
FE	1048	984	921	459	536	-1269	-1291	-1124	1054	739	-1133	-446	-165	-661	1986
Diff %	18	11	10	-18	2	12	8	9	-19	0	4	5	-101	34	18
							7° **loading**								
Experiment	538	605	733	331	443	-779	-965	-1024	766	617	-1131	-447	-157	-524	1028
FE	433	525	653	385	423	-690	-893	-942	847	605	-1052	-450	-221	-346	1239
Diff %	20	13	11	-16	5	11	7	8	-11	2	7	-1	-41	34	-21
							15° **loading**								
Experiment	-318	2	356	244	295	30	-412	-741	544	406	-990	-413	-244	-301	-89
FE	-283	5	331	292	281	36	-416	-711	587	426	-931	-437	-289	-191	305
Diff %	11	-167	7	-20	5	-18	-1	4	-8	-5	6	-6	-18	37	444

For the sensitivity analysis so to quantify the influence of the imprecise cement layer thickness we compare the strain values obtained by FE models with the cement layer to FE models in which the cement layer is zero (cement neglected).

Table B.8: FFM7R Imp: FE results for models with and without a cement layer. The values marked in red are untypical in their sensitivity to cement's presence (especially SG21).

	Strain [μstrain]										
	SG 11	**SG 12**	**SG 13**	**SG 21**	**SG 22**	**SG 23**	**SG 112**	**SG 113**	**SG 121**	**SG 122**	**SG 123**
						0° **loading**					
Cemented	1483	881	270	-1952	-1265	-728	482	285	191	-440	-554
Non Cemented	1519	922	305	-1713	-1277	-757	494	284	193	-307	-636
						7° **loading**					
Cemented	831	598	212	-1211	-889	-618	378	241	163	-370	-490
Non Cemented	888	622	234	-1017	-870	-622	391	241	165	-260	-562
						15° **loading**					
Cemented	80	264	143	-357	-444	-489	252	187	128	-277	-408
Non Cemented	167	268	149	-203	-399	-471	268	188	130	-203	-468

Table B.9: FFB1R Imp: FE results for models with and without cement.

	Strain [μstrain]													
	SG 11	**SG 12**	**SG 13**	**SG 14**	**SG 21**	**SG 22**	**SG 23**	**SG 111**	**SG 112**	**SG 113**	**SG 114**	**SG 121**	**SG 122**	**SG 123**
							0° **loading**							
Cemented	958	758	440	235	-856	-803	-630	265	244	178	179	-353	-316	-271
Non Cemented	959	730	429	247	-854	-812	-606	269	256	181	195	-348	-332	-278
							7° **loading**							
Cemented	226	329	282	179	-228	-388	-420	155	177	145	149	-235	-241	-233
Non Cemented	227	313	273	185	-227	-395	-405	154	188	149	162	-231	-253	-240
							15° **loading**							
Cemented	-561	-139	108	116	446	-38	-189	35	102	108	114	-106	-156	-188
Non Cemented	-560	-153	102	116	445	-31	-183	30	111	112	124	-101	-163	-194

Table B.10: FFB1L Imp: FE results for models with and without cement.

	Strain [μstrain]											
	SG 11	**SG 12**	**SG 13**	**SG 14**	**SG 15**	**SG 21**	**SG 22**	**SG 23**	**SG 112**	**SG 114**	**SG 122**	**SG 124**
						0° **loading**						
Cemented	861	770	572	171	192	-1096	-887	-468	287	247	-344	-451
Non Cemented	858	749	526	159	184	-1090	-875	-482	291	247	-332	-450
						7° **loading**						
Cemented	263	384	398	147	137	-527	-558	-361	216	211	-275	-409
Non Cemented	263	371	369	135	134	-528	-552	-373	215	210	-265	-407
						15° **loading**						
Cemented	-421	-68	195	111	80	132	-179	-240	126	163	-187	-349
Non Cemented	-423	-69	184	105	75	130	-174	-245	125	164	-183	-350

Table B.11: FFY Imp: FE results for models with and without cement.

	Strain [μstrain]										
	SG 11	**SG 12**	**SG 13**	**SG 21**	**SG 22**	**SG 23**	**SG 112**	**SG 113**	**SG 121**	**SG 122**	**SG 123**
					0° **loading**						
Cemented	1326	1001	480	-1475	-1281	-555	216	605	-410	-307	-636
Non Cemented	1335	1008	473	-1488	-1298	-548	220	603	-410	-302	-636
					7° **loading**						
Cemented	629	639	378	-813	-865	-458	176	516	-290	-260	-562
Non Cemented	632	643	372	-821	-878	-453	180	514	-289	-257	-563
					15° **loading**						
Cemented	-188	215	255	-53	-375	-340	128	404	-148	-203	-468
Non Cemented	-180	215	250	-44	-383	-336	130	403	-145	-201	-468

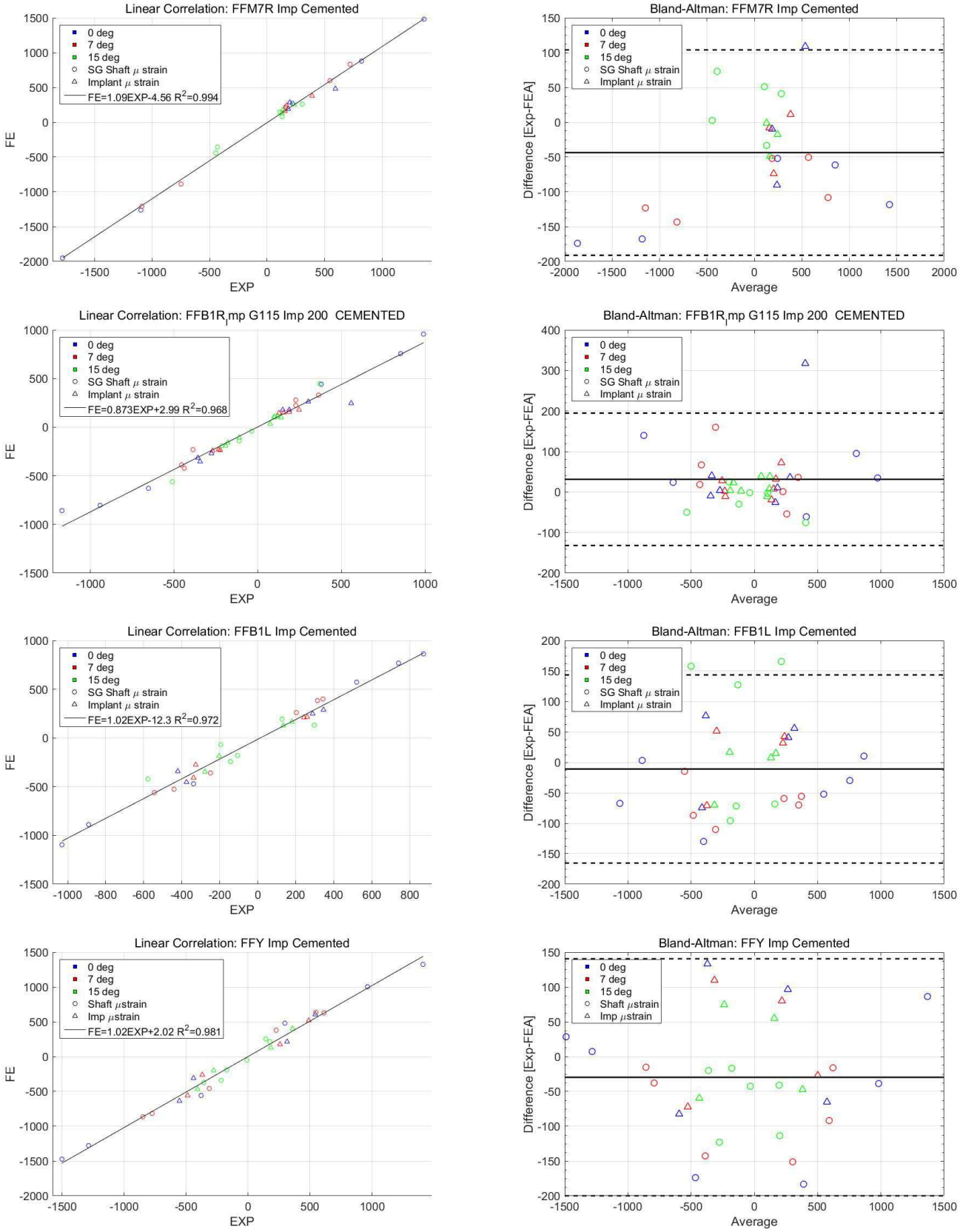

Figure B.10: LC and BA plots for all four implanted femurs

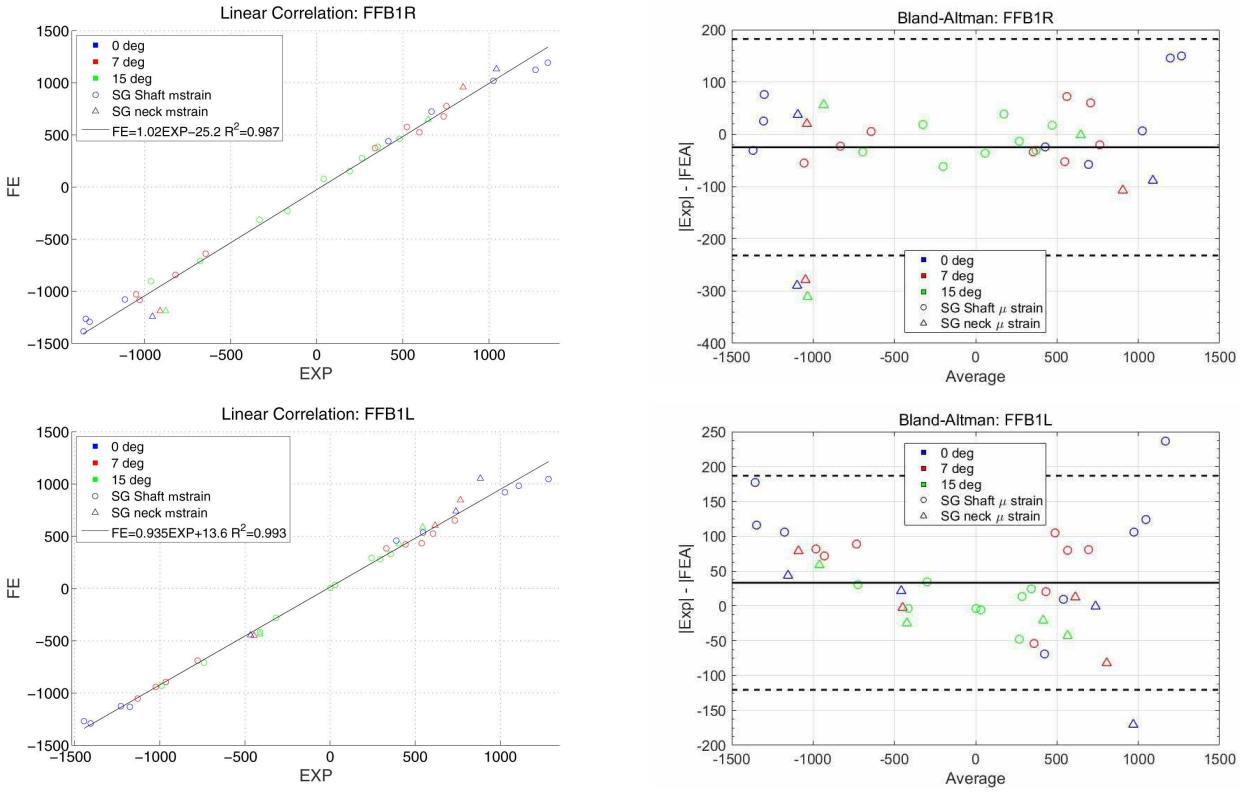

Figure B.11: LC and BA plots for FFB1 intact femurs